remote sensing

Article

Modeling Soil CO_2 Efflux in a Subtropical Forest by Combining Fused Remote Sensing Images with Linear Mixed Effect Models

Xarapat Ablat [1,2], Chong Huang [2], Guoping Tang [1,*], Nurmemet Erkin [3] and Rukeya Sawut [4]

[1] School of Geography and Planning, Sun Yat-Sen University, Guangzhou 510275, China
[2] State Key Laboratory of Resources and Environmental Information System, Institute of Geographic Sciences and Natural Resources Research, Chinese Academy of Sciences, Beijing 100101, China
[3] College of Resource and Environment, Xinjiang Agricultural University, Urumqi 830052, China
[4] College of Geographic Science and Tourism, Xinjiang Normal University, Urumqi 830054, China
* Correspondence: tanggp3@mail.sysu.edu.cn

Abstract: Monitoring tropical and subtropical forest soil CO_2 emission efflux ($FSCO_2$) is crucial for understanding the global carbon cycle and terrestrial ecosystem respiration. In this study, we addressed the challenge of low spatiotemporal resolution in $FSCO_2$ monitoring by combining data fusion and model methods to improve the accuracy of quantitative inversion. We used time series Landsat 8 *LST* and *MODIS LST* fusion images and a linear mixed effect model to estimate $FSCO_2$ at watershed scale. Our results show that modeling without random factors, and the use of Fusion *LST* as the fixed predictor, resulted in 47% (marginal R^2 = 0.47) of $FSCO_2$ variability in the Monthly random effect model, while it only accounted for 19% of $FSCO_2$ variability in the Daily random effect model and 7% in the Seasonally random effect model. However, the inclusion of random effects in the model's parameterization improved the performance of both models. The Monthly random effect model that performed optimally had an explanation rate of 55.3% (conditional R^2 = 0.55 and t value > 1.9) for $FSCO_2$ variability and yielded the smallest deviation from observed $FSCO_2$. Our study highlights the importance of incorporating random effects and using Fusion *LST* as a fixed predictor to improve the accuracy of $FSCO_2$ monitoring in tropical and subtropical forests.

Keywords: forest soil carbon emission; multisource remote sensing fusion; land-atmosphere interactions; regional earth system simulation; tropical and subtropical forests

check for updates

Citation: Ablat, X.; Huang, C.; Tang, G.; Erkin, N.; Sawut, R. Modeling Soil CO_2 Efflux in a Subtropical Forest by Combining Fused Remote Sensing Images with Linear Mixed Effect Models. *Remote Sens.* **2023**, *15*, 1415. https://doi.org/10.3390/rs15051415

Academic Editor: Bassil El Masri

Received: 22 January 2023
Revised: 22 February 2023
Accepted: 27 February 2023
Published: 2 March 2023

1. Introduction

Forest soil CO_2 emission ($FSCO_2$) serves as a crucial conduit in the global carbon cycle and exerts a significant impact on the carbon budget of terrestrial ecosystems. In recent decades, the continuous increase in greenhouse gases in the atmosphere has changed forest growth and productivity, resulting in the acceleration of carbon dioxide emissions from soil to the atmosphere [1]. Therefore, timely and accurate observation of $FSCO_2$ at large spatial scales has significant scientific value for deeply revealing the mechanism of the global carbon cycle and for precisely predicting future climate change.

There are many $FSCO_2$ monitoring methods, among which the Box method is widely used [2]. Although the automatically closed gas chamber can effectively obtain the change of $FSCO_2$ in time, most gas chambers still need to fix the spatial difference of $FSCO_2$ monitoring at the regional or landscape scale. In addition, due to the lack of long-time-series field observation of $FSCO_2$, earth observation images cannot directly monitor the temporal and spatial variation of $FSCO_2$, which limits the direct prediction of $FSCO_2$ through remote sensing products [3]. Therefore, previous studies estimated $FSCO_2$ indirectly through biotic and abiotic factors, among which soil temperature is the key environmental factor to control $FSCO_2$ [4]. These studies mainly investigated interconnections between soil temperature and carbon release from the land surface from different aspects [5–7].

Remote-sensing-based land surface temperature (*LST*) measurement has great potential for obtaining the spatial distribution characteristics of *$FSCO_2$* at the pixel level [1,8–10]. The *MODIS LST* product is one of the successful examples. It is currently widely used in monitoring large-scale *$FSCO_2$* around the world [11]. The split window algorithm, used for inverting this product, can effectively compensate for atmospheric attenuation. However, the limitation in spatial resolution of *MODIS LST* restricts its applicability at small, regional scales. Landsat 8 addresses the shortcomings of *MODIS LST* products and provides an unprecedented opportunity to improve the accuracy of *LST* measurement via remote sensing inversion. Several case studies have used the split window algorithm to obtain *LST* from Landsat 8 [12–15]. However, a recent report shows that the thermal band 11 of Landsat 8 is subject to relatively high levels of stray light interference, which induces caution in using a split window algorithm [16]. Therefore, the data fusion algorithm has been used to estimate *LST* from single-channel TIRS images [17–20]. Although the quality of *LST* data with different temporal and spatial resolutions has been improved greatly, the mapping of *$FSCO_2$* based on the improved *MODIS* and Landsat 8 *LST* remote sensing fusion data is still scarce.

The aim of this study is to address the following scientific problems in estimating the *$FSCO_2$* at high spatiotemporal scale: first, how to retrieve a high-quality spatiotemporal data set of remote sensing-based *$FSCO_2$* observation variables; second, how to construct an efficient estimation model using multisource satellite-based data combined with an *$FSCO_2$* model. The solution to this problem is valuable for accurately estimating the global carbon budget, mitigating global warming, and accurately predicting future climate change.

2. Materials and Methods

2.1. Study Basin

The study area (23.67–23.96°N, 114.03–113.75°E) is a headwater catchment of the Liuxihe (LXH) River basin, named the LXH Reservoir watershed, and located in the northern part of Guangdong Province of China [21] (Figure 1). It is characterized by a typical subtropical monsoon climate with long-term mean annual temperature of 20.3 °C and precipitation of 2100 mm [22]. The rainfall is concentrated in the period from March to September (about 80%). The rest of the months are part of the dry period in this basin, mainly consisting of autumn and winter. The catchment covers 456.7 km^2, and the altitude ranges from about 150 m to more than 1140 m. As one of the major head water reservoir basins in southern China, it supplies drinking water to the city of Guangzhou and thus is an important ecological barrier in the north of Guangzhou [23]. Vegetation cover, mainly forests, accounts for 80% (365.4 km^2) of the catchment area. The main vegetation types are broad-leaf and needle-leaf evergreen forests. We selected Chenhedong (CHD) Nature Reserve and GuoYuan (GY) in the LXH National Forest Park as sampling points and conducted 10 independent measurements of the *$FSCO_2$* at each.

2.2. Data Processing

2.2.1. Earth Observation Data Sets and Preprocessing

The remote sensing data employed in this study consist of Landsat 8 images and Land Surface Temperature (*LST*) products derived from daily Moderate Resolution Imaging Spectroradiometer (*MODIS*) images. The *MODIS LST* product (MOD11A2) was obtained from the Oak Ridge National Laboratory Distributed Active Archive Center (DAAC) (http://MODIS.ornl.gov/cgi-bin/MODIS) while the Landsat 8 images were downloaded from the US Geological Survey (USGS) website for free (http://Landsat.usgs.gov). A total of 70 *MODIS LST* products and 7 Landsat images (Table 1) with low cloud coverage in the study region (>1%) were used.

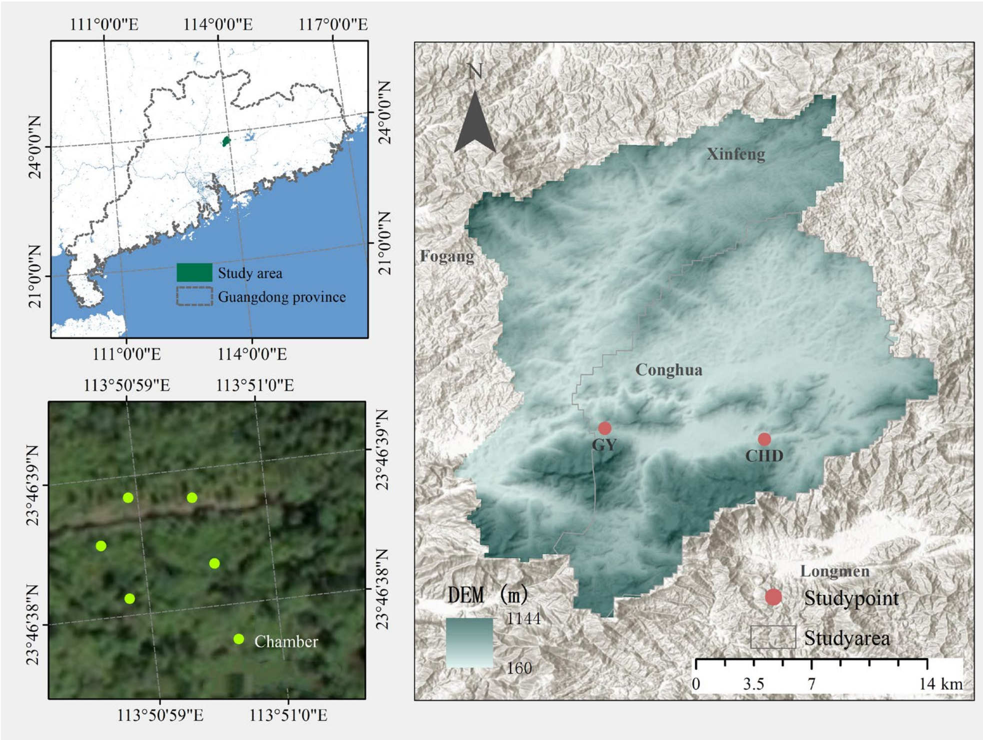

Figure 1. The location of the Liuxihe (LXH) watershed in Guangzhou province of China (**upper left**). The Guoyuan (GY) and Chenhe Dong (CHD) sampling sites in LXH watershed (**right**). The distribution of chambers in each study site, base map from Google Earth (**lower left**).

Table 1. Metadata for Landsat 8 images.

Date	Cloud Cover (%)	Azimuth/Zenith Angles of the Sun	$M_{L(10)}$	$A_{L(10)}$	K_1	K_2
11 September 2019	0	135.06/58.8	3.34×10^{-4}	0.1	774.89	1321.08
27 September 2019	5.9	139.15/57.0	3.34×10^{-4}	0.1	774.89	1321.08
29 October 2019	1.5	151.85/47.8	3.34×10^{-4}	0.1	774.89	1321.08
14 November 2019	0.3	154.61/43.4	3.34×10^{-4}	0.1	774.89	1321.08
30 November 2019	52.3	155.31/39.9	3.34×10^{-4}	0.1	774.89	1321.08
17 January 2020	91.3	149.15/38.2	3.34×10^{-4}	0.1	774.89	1321.08
18 February 2020	0	141.45/45.3	3.34×10^{-4}	0.1	774.89	1321.08

$M_L(10)$ is the multiplicative rescaling factor; $A_L(10)$ is the additive rescaling factor; K_1 and K_2 are thermal constants; Cloud cover represents the cloud coverage of a scene of Landsat 8 image.

We collected *MODIS LST* products of day and night spanning from 28 September 2019 to 4 January 2020. Filtering and clipping of images were complemented before usage. Landsat 8 images without cloud cover in the study area were collected for the study period (row 122 and path 43). In order to counteract the influence of stray light on the thermal band 11 of Landsat 8, this study utilized thermal band 10 (with a spatial resolution of 100 m) for estimating *LST*.

2.2.2. Field-Observed Data and Preprocessing

The field measurements of $FSCO_2$ were conducted using a closed chamber in each study site (GY and CHD) during the study period (Figure 1). $FSCO_2$ at an interval of two times per month for each site was measured using an automatic cavity ring-down spectrophotometer [22]. There was no special setting for the instrument in this study, and the default company settings are kept for reference [24].

Furthermore, in situ measurements of soil temperature, soil moisture, air temperature, and precipitation were also conducted. Specifically, soil temperature (ST) and moisture (SM) were measured at soil depths of 5–10 cm in the vicinity of the chamber sampling site using a heat dissipation probe (TDP, Dynamax Inc., Houston, TX, USA) at three different locations [22]. The mean values of these variables were obtained by averaging repeated measurements at each site.

2.3. Methods

Figure 2 illustrates the specific technical methods used in this study. To improve the precision and accuracy of monitoring the carbon release flux from forest soils in the study area, high-quality spatiotemporal remote sensing fusion images were obtained, and the LXH headwater watershed in the humid region of South China was selected as the research area. High temporal and spatial remote sensing forest soil CO_2 emission flux parameters were retrieved, and the new fusion algorithm and the CO_2 emission flux estimation model were effectively coupled to construct the multi-state variable optimization model.

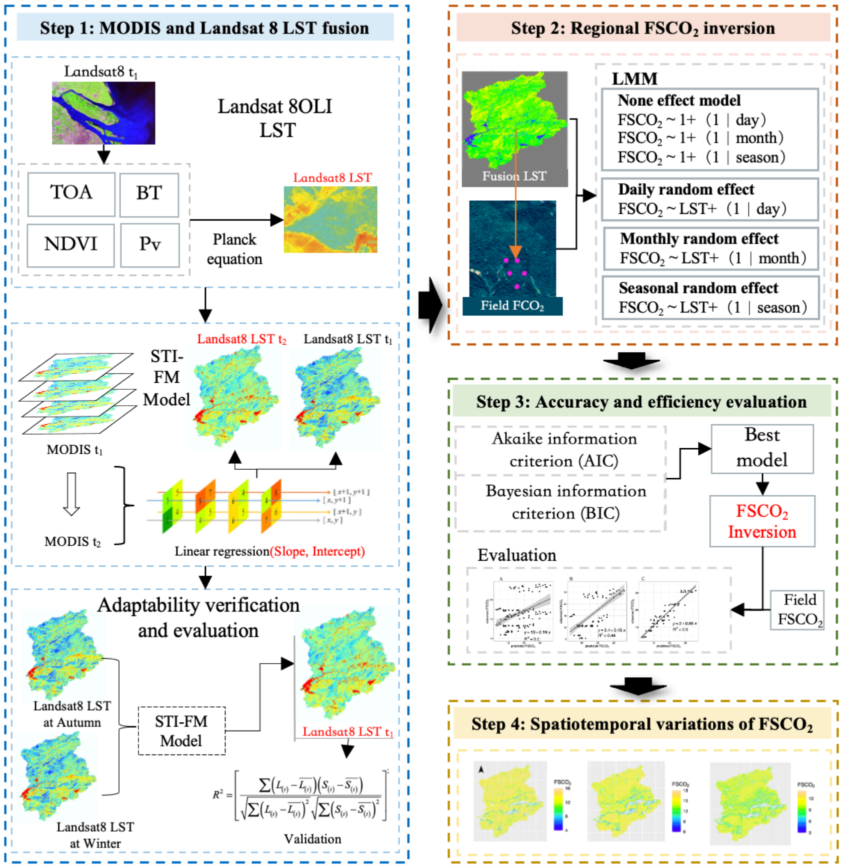

Figure 2. The flowchart of the research.

Finally, the field measurements of $FSCO_2$ and high-quality spatiotemporal remote sensing parameter sets of carbon flux were used for accuracy assessments of the forest soil CO_2 emission in different models, which improved the accuracy and efficiency of regional CO_2 emission flux estimation.

2.3.1. Landsat 8 *LST* Calculation

In order to analyze the data effectively, we used a set of mathematical equations to process the raster images using a raster image calculator (Raster calculation tool within ArcMap 10.8). Landsat band 4, band 5, and thermal band 10 were used. Band 4 and band 5 used for calculating the Normalized Difference Vegetation Index (*NDVI*). There are six steps for estimating Landsat 8 *LST* [25–27] and they are described below.

(1) The calculation of top-of-atmosphere radiance (TOA): The digital number (DN) of each pixel in the original Landsat 8 images was used to calculate the TOA radiance of the corresponding pixel according to the following formula provided by USGS:

$$TOA_{\lambda} = M_L \times Q_{cal} + A_L \tag{1}$$

where TOA_{λ} represents the TOA (W m^{-2} srad μm); M_L is the band 10-specific multiplicative rescaling factor; Q_{cal} is the DN values of band 10; and A_L corresponds to the band-specific additive rescaling factor. The values for the above required parameters are available from the metadata file.

(2) The conversion of TOA to brightness temperature (BT): The TOA radiance was converted to BT by Equation (2):

$$BT = K_2/(ln((K_1/TOA) + 1)) - 273.15 \tag{2}$$

where K_2 and K_1 represent the specific band thermal conversion constants, respectively. To obtain results in degrees Celsius, the radiation temperature needs to be adjusted by adding absolute zero (about—273.15 °C).

(3) The $NDVI$ calculation: The calculation of $NDVI$ is important because the vegetation proportion (P_v) is highly related to $NDVI$ and the emissivity (ε) that is related to P_v can be calculated.

$$NDVI = \frac{(b_5 - b_4)}{(b_5 + b_4)}, \tag{3}$$

where $NDVI$ is the Normalized Difference Vegetation Index and b_5 and b_4 represent the fifth band (0.845–0.885 μm) and the fourth band (0.630–0.680 μm) of the Landsat 8 images, respectively.

(4) The vegetation proportion calculation:

$$P_v = square\left(\frac{(NDVI - NDVI_{min})}{(NDVI_{max} - NDVI_{min})}\right) \tag{4}$$

where $NDVI_{min}$ is the minimum value of $NDVI$ and $NDVI_{max}$ is the maximum value of $NDVI$.

(5) Emissivity calculation:

$$\varepsilon = 0.004 \times P_v + 0.986 \tag{5}$$

(6) LST estimation:

$$LST = \frac{BT}{\left(1 + \left(\frac{0.0015 \times BT}{1.4388}\right) \times ln(\varepsilon)\right)} \tag{6}$$

All calculations were completed using the ArcGIS raster calculation tools.

2.3.2. Field Measurements and Validation

The sampling sites were ensured not to be covered by vegetation before measurement, and the chamber was required to be close to the ground to ensure accurate reading of carbon flux. We inserted the chamber into the surface soil to a depth of 3–5 cm. The instrument recording time for each chamber was adjusted to 1 s, and the measurement time interval was 2–5 min, repeated five times. Due to the difference in daily variation of $FSCO_2$, the measurements between 10:00 AM to 3:00 PM (local time) were selected and used as the field monitoring $FSCO_2$ data in this study. The final $FSCO_2$ calculation equation [28] is as follows:

$$FSCO_2 = \rho \times \frac{V}{S} \times \frac{\Delta C}{\Delta T} \tag{7}$$

where the $FSCO_2$ is the carbon release between the land surface and air in forest soil (g C·m^{-2}·day^{-1}); ρ is the density of CO_2; S and V represent the area (m^2) and the volume (m^3) of the chamber, respectively; ΔC is the changing trend of CO_2 concentration in soil with time; and ΔT is the time interval. We randomly selected 70% of $FSCO_2$ data for model operation, and the remaining 30% were used for model validation.

2.3.3. STI-FM Fusion Model and Validation

The STI-FM model is a fusion method proposed by Khaled hazaymeh in 2015 [17]. The aim of the model is to use two different sources of satellite remote sensing images to generate high-quality spatiotemporal resolution fusion products. The model is based on two assumptions. First, there is a linear relationship between two inconsistent *MODIS LST* images; and second, the *LST*s obtained from Landsat 8 and *MODIS* images at a specific time (such as T_1 or T_2) are similar. The core idea of the model is to use the linear relationship between the two *MODIS LST* products to generate Landsat 8 *LST* prediction data of high time series. In other words, the model uses the linear relationship between the *MODIS LST* in T_1 and T_2 to generate a synthetic Landsat 8 *LST* image in T_2 using the Landsat 8 *LST* image in T_1.

$$MODIS(T_2) = a \times MODIS(T_1) + c \tag{8}$$

$$Synth\_L8(T_2) = a \times L8(T_1) + c \tag{9}$$

where $MODIS(T_2)$ and $MODIS(T_1)$ are two consecutive *MODIS LST* images; a and c are the slope and intercept between the $MODIS(T_2)$ and $MODIS(T_1)$, respectively; $L8(T_1)$ is the Landsat 8 image collected from the same time with $MODIS(T_1)$; and $Synth\_L8(T_2)$ is the fusion image in T_2 at the same time and spatial resolution as $L8(T_1)$.

Hazaymeh applied the STI-FM model to the semi-arid area of the Middle East and Jordan [17]. When applying it to the subtropical monsoon climate region, it is necessary to verify the applicability of the model. Previously, scholars applied the model to the Great Bay area of Guangdong, Hong Kong, and Macao and verified its feasibility [16]. The model was performed in the Google Earth Engine (GEE) platform, using R language and ArcGIS 10.8 software. The accuracy of the model is evaluated by assessing the adjusted R^2 and root mean square error ($RMSE$) using R language.

$$R^2 = \left[\frac{\sum\left(L_{(t)} - \overline{L}_{(t)}\right)\left(S_{(t)} - \overline{S}_{(t)}\right)}{\sqrt{\left(\sum L_{(t)} - \overline{L}_{(t)}\right)^2}\sqrt{\left(\sum S_{(t)} - \overline{S}_{(t)}\right)^2}} \right]^2 \tag{10}$$

$$RMSE = \sqrt{\frac{\sum\left[S_{(t)} - L_{(t)}\right]^2}{n}} \tag{11}$$

where $L_{(t)}$ is the actual Landsat 8 *LST* value; $S_{(t)}$ is the Landsat 8 *LST* value synthesized by the model; $\overline{L}_{(t)}$ is the average value of the actual Landsat 8 *LST*; $\overline{S}_{(t)}$ is the average value of Landsat 8 *LST* synthesized by the model; and N = 10,000.

2.3.4. $FSCO_2$ Estimation and Validation

The estimation of $FSCO_2$ based on remote sensing data involves the following three steps: Firstly, a normality test is conducted on the field-measured $FSCO_2$ data and the fused *LST* product test to explore seasonal, monthly, and daily changes of $FSCO_2$. Then, the constrained maximum likelihood method is applied to establish three linear mixed effect models under different time scales (season, month, and day). The linear mixed models include the null model, where the random intercept as a fixed predictor is grouped according to the level of daily and monthly factors, and the Daily random effect model, where the fusion of remote-sensing-derived *LST* is used as a fixed predictor and the daily factor level is used as a random intercept effect. The fusion remote sensing *LST* as a fixed predictor plus the daily factor level provides a random intercept effect; the composition of the Monthly random effect model and Seasonally random effect models are similar to that of the Daily random effect model, but the monthly and seasonal factor levels are used as the random intercept effects, respectively, in the two models. Lastly, the three models were compared with their corresponding null models utilizing the Akaike information criterion (AIC) and Bayesian information criterion (BIC) to select the best optimum model.

Marginal R^2 (mR^2) and conditional R^2 (cR^2) were used to evaluate these models in estimating seasonal, monthly, and daily $FSCO_2$ [29]. Marginal R^2 quantifies the proportion of variance explained by the fixed prediction of Landsat 8 *LST*, while condition R^2 evaluates the proportion of variance captured by the fixed prediction of Landsat 8 *LST* and the seasonal, monthly, and daily factor levels (random factors). The accuracy and efficiency of the Daily random effect model, Monthly random effect model, and Seasonally random effect model were evaluated using the validation data set. The accuracy of these models was evaluated by assessing their adjusted R^2 and *RMSE*.

3. Results

3.1. Field-Measured $FSCO_2$ and Related Environmental Variables Analysis

Figure 3 shows the seasonal and daily changes in $FSCO_2$ in the CHD and the GY. It is evident that there are significant seasonal differences in $FSCO_2$ at both study sites, with higher values in autumn than in winter (Figure 3 CHD Season and GY Season). Additionally, the average $FSCO_2$ values in Site site GY are smaller than that in site CHD, indicating that $FSCO_2$ in the study area varies both temporally and spatially. When abnormal values are excluded, the $FSCO_2$ in GY during the dry season ranges from 0.15 to 39.36 g C m^{-2} day^{-1}, with an average of 7.83 g C m^{-2} day^{-1}. In contrast, the $FSCO_2$ in CHD during the dry season ranges from 0.97 to 41.09 g C m^{-2} day^{-1}, with an average of 12.73 g C m^{-2} day^{-1}. This indicates that the $FSCO_2$ values in the study sites are spatially heterogeneous, depending on time and space.

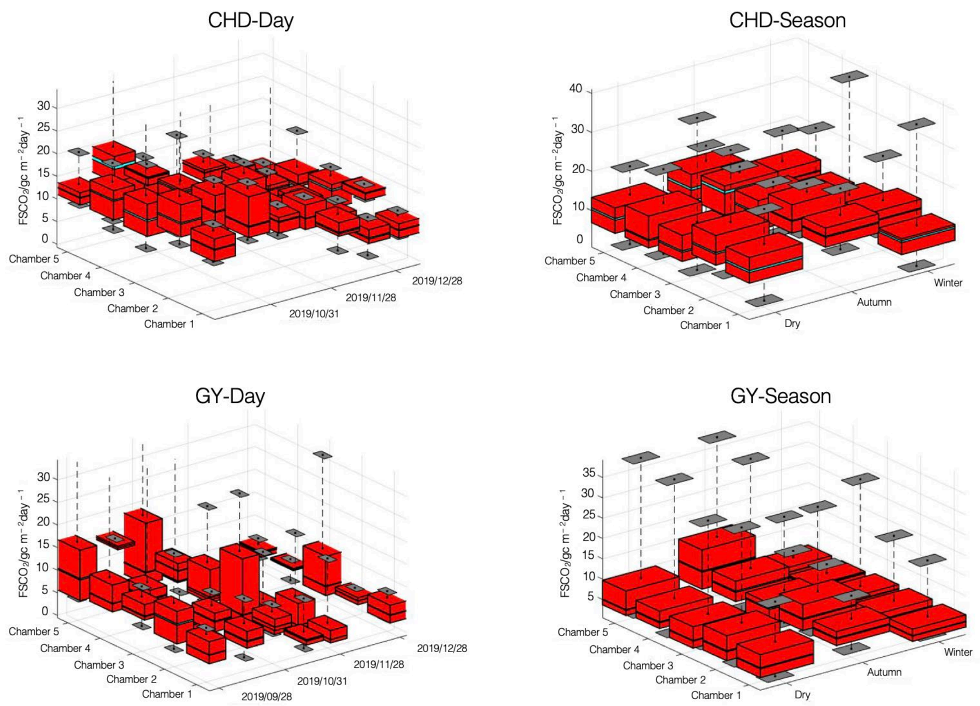

Figure 3. The monthly and daily variation of field-measured $FSCO_2$ in GY and CHD sites.

Figure 4 shows the relationship between the field-measured $FSCO_2$ and the soil respiration, topsoil temperature, air temperature, and relative humidity. Results show that the correlation coefficients between the $FSCO_2$ and surface air temperature in the GY and CHD sites are 0.46 ($p < 0.001$) and 0.70 ($p < 0.001$), respectively. The topsoil temperature in the GY and CHD sites has stronger positive correlation with the $FSCO_2$ ($R^2 = 0.72$ and $R^2 = 0.70$) at the 0.001 significance level. $FSCO_2$ is also significantly correlated with the relative humidity in GY; the correlation coefficient is 0.4. The results also show that changes in soil respiration do not have a noticeable impact on the level of $FSCO_2$, and that soil temperature and near-surface air temperature are crucial environmental factors affecting the $FSCO_2$ in the subtropical forest during the dry season.

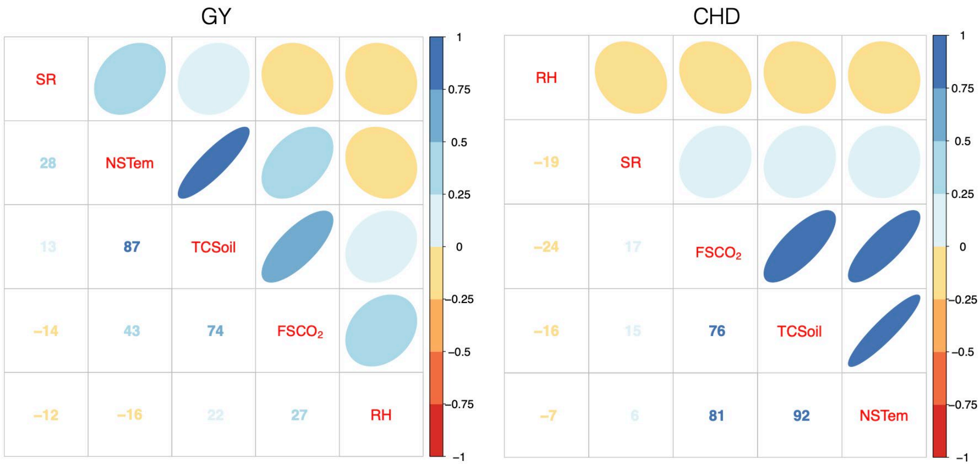

Figure 4. Relationship between the field-measured $FSCO_2$ and abiotic variables (SR: Soil respiration, TC Soil: Topsoil temperature, TAmbient-Avg: Daily average near-surface temperature, RH: relative humidity) in GY and CHD.

3.2. Multisource Remote Sensing LST Fusion

3.2.1. Fusion LST Datasets and Accuracy Assessment

Figure 5A shows a qualitative comparison of Landsat 8 *LST* and Fusion *LST* images on 28 September 2019, highlighting their similarity in features. The study also investigated *LST* at three different elevations during the study period and found that the Fusion *LST* image accurately predicted *LST* in variable topographic conditions. Histograms were generated for actual Landsat 8 *LST* and Fusion *LST* images for the entire study area and revealed their similarities (Figure 5B). For quantitative evaluation, Fusion *LST* and MYD *LST* of the entire study area were plotted on 28 September 2019, and further Fusion *LST* and topsoil temperature in sampling chamber points were plotted during the study period (Figure 5C,D). Strong relationships were found between the variables of interest, with R^2 values of 0.77 and 0.60, and RMSE values of 0.33 and 2.24, respectively. Additionally, the close relationship between the regression line of MYD-*LST* and Fusion *LST* and the 1:1 line indicates a strong correlation between the two datasets.

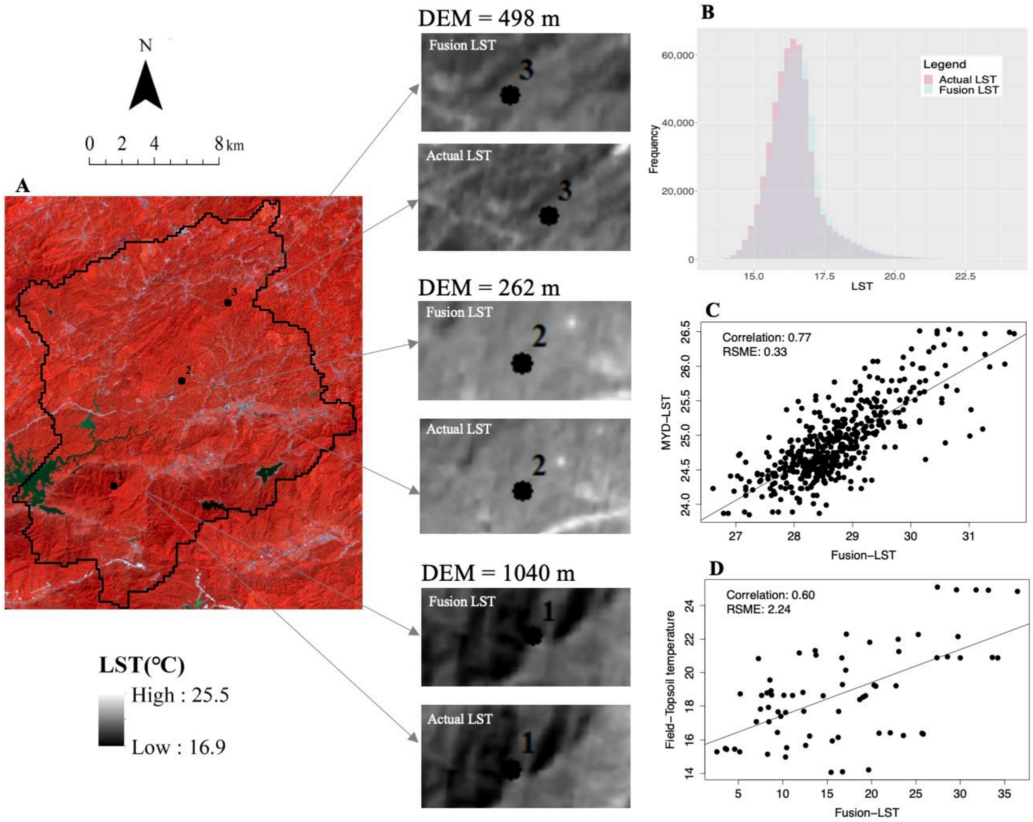

Figure 5. Comparison between the Fusion *LST* and actual Landsat 8 *LST* at different altitudes (DEM = 498 m, 262 m, 1040 m) of study area on 28 September 2019 (**A**). The histogram plot of Fusion *LST* and Landsat 8 *LST* (**B**). Relationship between the MYD-*LST* and Fusion *LST* (**C**) and relationship between the field based topsoil temperature and Fusion *LST* (**D**).

3.2.2. The Spatiotemporal Variations of *LST* in Landsat 8 *LST*, *MODIS LST* and Fusion *LST*

Spatial variations of *LST* show that the distribution of $FSCO_2$ has significant spatial patterns in all three multisource remote sensing *LST* images in different study periods and that surface topography is the major factor responsible for the spatial variations of $FSCO_2$: as the altitude rises, the *LST* decreases. The *LST* variations also significantly differ during different seasons of the year. The monthly mean temperatures of September, October, and December during the dry season are 25 °C, 20 °C, and 15 °C in the study region (Figure S1), respectively. Moreover, compared with the *MODIS LST* (500 m), the Fusion *LST* (100 m) has significantly higher spatial resolution, which improved markedly the $FSCO_2$ estimation at large regional scale. The accuracy of fusion *LST* data satisfied the conditions for simulating $FSCO_2$.

Figure 6 shows the spatiotemporal changing patterns of *LST* in autumn, winter, and the dry seasons as detected by Landsat and *MODIS* images and Fusion *LST* products of the study area. The figure illustrates that there is considerable variation in the accuracy of slope when using multisource satellite remote sensing products. The changing trends of *LST* at the pixel level obtained using Landsat images have higher spatial resolution, but the trend analysis is not accurate due to the low time resolution. This suggests that using a combination of satellite imagery from different sources can improve the accuracy of *LST* mapping, but the low time resolution of the images may still affect the accuracy of the results.

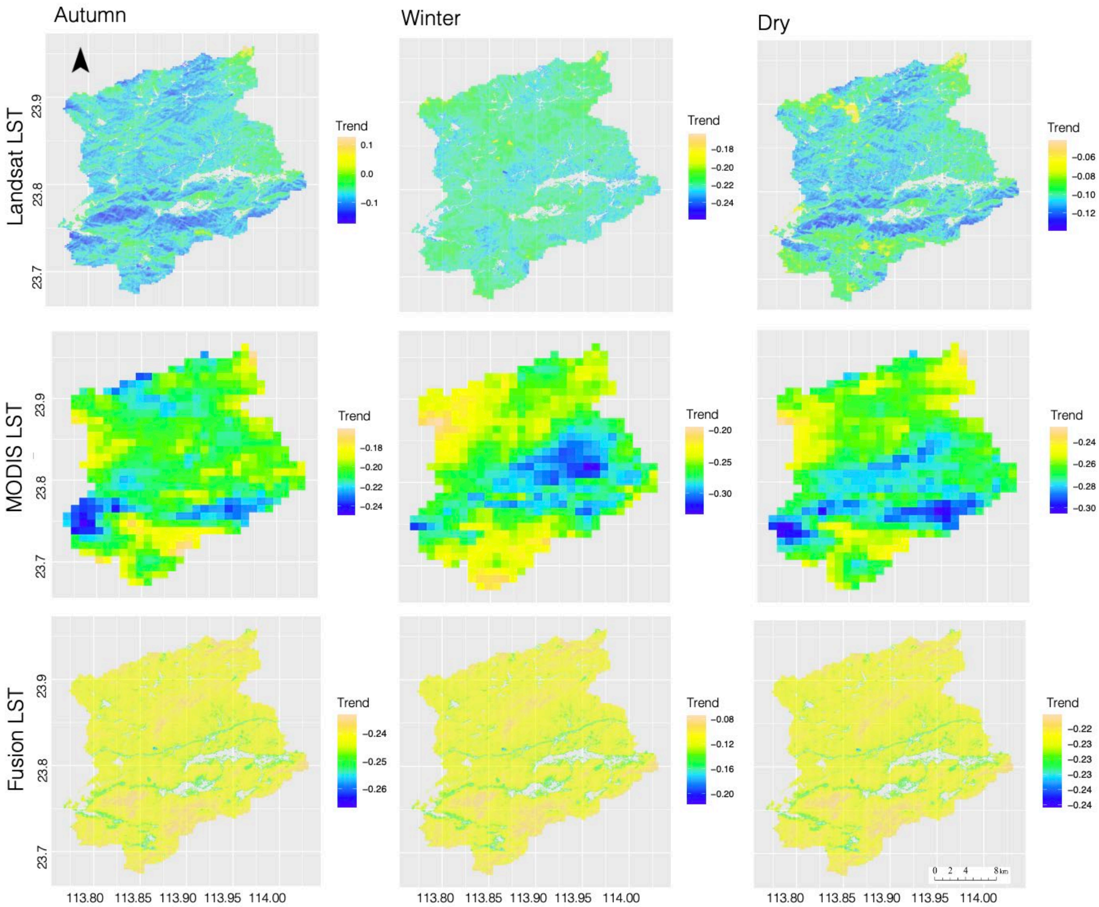

Figure 6. The dynamics of the land surface temperature (*LST*) in the subtropical forest derived from multisource remote sensing images in autumn, winter, and dry seasons. The three panels in the first row are derived from Landsat 8 *LST* images; the three panels in the second row are derived from *MODIS LST* images; the three panels in the third row are derived from Landsat-*MODIS* Fusion *LST*.

Furthermore, Figure 6 shows the trends of *LST* in the subtropical forests in different seasons. The changing slopes of *LST* in winter are larger than in autumn, which is likely due to the significant decrease in *LST* in subtropical forests during the winter season. The spatial distribution of the trend variance in *LST* reveals distinct patterns over different periods. Specifically, the results indicate that *LST* in high-altitude areas differs more significantly across space compared with low-altitude areas. This is likely because the forest canopy in high-altitude areas is denser than in low-altitude areas, resulting in *LST* being more similar to near-surface air temperature. As a result, the changing dynamics of *LST* in high-altitude areas are more significant than in low-altitudinal areas.

3.3. *$FSCO_2$ Simulation*

3.3.1. The Construction of the Linear Mixed Based $FSCO_2$ Inversion Model

The similarities in variance between the Fusion *LST* variable and residual variance across different months indicate that the changes in Fusion *LST* are mainly caused by random factors rather than by other fixed factors (Table S1). The degree of change in Fusion *LST* across different months is relatively small (0.04) in the observed data, and this difference is mainly due to random error, suggesting that the variations in Fusion *LST* between months are mainly caused by random factors such as measurement error. Additionally, the differences in Fusion *LST* between months account for 46.8% of the total variability in the data, and the remaining variability can be explained by random errors in the model.

For the fixed effect, the slope parameter of 0.21 and the intercept of 0.54 suggest that there is a linear relationship between the independent and dependent variables. The data indicate that there is a significant difference ($p < 0.001$) in mean Fusion $FSCO_2$ between measurements taken from September to January in the dry season. Additionally, the variance in Fusion LST within months is relatively low (0.03) compared with the variance between autumn and winter (0.05). This suggests that there is less variation in Fusion LST within each month than between autumn and winter. It is noticeable that the variation of Fusion LST by month accounted for 34.5% of the error left in the model, indicating that when the predictor variable (Fusion LST) is grouped by autumn and winter, there is no significant difference in $FSCO_2$ measurement between autumn and winter. This also suggests that the Fusion LST model does not vary significantly between these two seasons. It means that the model is effective in explaining the variance in Fusion $FSCO_2$ between months, but less effective in explaining the variance between autumn and winter (Table S2).

The variance in Fusion LST between days was high (variance = 0.07) compared with that within months (variance = 0.007). This suggests that there is more variation in Fusion LST between days than within each month. The variation of Fusion LST by day accounted for 9.72% of the error left in the model. For the fixed effect, the slope parameter was 0.13 while the intercept was 0.48. This suggests that there is a linear relationship between the independent and dependent variables, but the slope of 0.13 is relatively small, which means that the change in dependent variable is not large for one unit change in the independent variable. The intercept is 0.48, which means when the independent variable is zero, the dependent variable has a value of 0.48. The result also states that there is no significant difference ($p < 0.42$) in mean Fusion $FSCO_2$ measurements. This means there is not enough evidence to show that a meaningful difference in the mean Fusion $FSCO_2$ measurements between different groups or conditions exists. In other words, it suggests that the model is not effective in explaining the variance in Fusion $FSCO_2$ measurements between days and within months, and that the data do not provide enough evidence for a meaningful difference in the mean Fusion $FSCO_2$ measurements between different groups or conditions (Table S3).

3.3.2. Model Validations

Table 2 shows the performance of the Daily random effect model, Monthly random effect model, and Seasonally random effect model in comparison with their respective null models and in comparison with each other. The results indicate that the Daily random effect model and Monthly random effect model comparatively have lower AIC and BIC values than the Seasonally random effect model. This suggests that the Daily and Monthly models have better explanatory power and are more parsimonious than the seasonal model. Meanwhile, the Daily random effect model and Monthly random effect model were significantly improved over the intercept-only model.

Table 2. Evaluation of linear mixed effect models, outlined by random intercept and Fusion LST segmented by day (between 28 September 2019 to 4 January 2020), month (September, October, November, December, and January), and season (Autumn, Winter and Dry) of the year. Models were assessed using the Akaike information criterion (AIC), Bayesian information criterion (BIC), the p-value of a chi-squared test, and both marginal and conditional R-squared (mR^2 and cR^2).

Model Type	Model Description	AIC	BIC	p-Value	mR^2	cR^2
None random effect	$FSCO_2$~1 + (1 | day)	-	-	-		
	$FSCO_2$~1+ (1 | month) $FSCO_2$~1 + (1 | season)	-	-	-		
Daily random effect	$FSCO_2$~LST + (1 | day)	220.75	208.99		0.19	0.904
Monthly random effect	$FSCO_2$~LST + (1 | month)	−34.76	−23.00	<0.001	0.47	0.553
Seasonally random effect	$FSCO_2$~LST + (1 | season)	984.47	996.24	<0.217	0.07	0.353

The results of a statistical analysis of three different models indicate that the use of fixed predictors (such as Daily, Monthly, and Seasonally) can explain variations in the dependent variable ($FSCO_2$) (Table 2). For example, the three models performed differently in terms of how well their fixed predictors (mR^2) or combination of fixed predictors and random factors (cR^2) explained the variations in $FSCO_2$. The fixed predictor of the Daily random effect model captured 19% of the variability in $FSCO_2$, the Monthly random effect model explained 47%, and the Seasonally random effect model explained 7%. However, when the proportions of variance captured by fixed predictors and random factors were combined, the Daily random effect model performed better than the Monthly and Seasonally random effect models. The former could explain 90.4% of the total variance in the model, while the Monthly random effect model and Seasonally random effect model explained only 55.3% and 35.3%, respectively. It is noteworthy that the Daily random effect model and Seasonally random effect model do not deviate from the assumption of common variance of linear regression models. A likelihood-ratio test showed that there was no statistically significant difference between a heteroscedastic model and each of the Monthly random effect model, Daily random effect model, and Seasonally random effect model.

A detailed analysis of the results showed that the discrepancies between the estimated values and the actual observed $FSCO_2$ varied depending on which model was used (Figures 7 and 8). This indicates that the three models had different levels of accuracy in explaining the variations of the dependent variable of $FSCO_2$. Before $FSCO_2$ reached 0.5 g C m^{-2}/day^{-1}, the Daily random effect model overestimated $FSCO_2$. When $FSCO_2$ reached 0.75 g C m^{-2}/day^{-1} in the Monthly random effect model, $FSCO_2$ values were estimated properly in the Seasonally random effect model. Consequently, the Daily random effect model produces an RMSE of 0.22, while the RMSE is 0.28 in the Monthly random effect model and 0.9 in the Seasonally random effect model. Although the Daily random effect model and the Monthly random effect model exhibited similar RMSE, the Daily random effect model demonstrated a stronger correlation between the estimated and observed $FSCO_2$ than the Monthly random effect model (adjusted R^2 = 0.44, 0.9, and 0.19 for the Daily random effect model, Monthly random effect model, and Seasonally random effect model, respectively) (Figure 7). The Monthly random effect model that performed optimally had an explanation rate of 55.3% (conditional R^2 = 0.55 and t value > 1.9) for $FSCO_2$ variability and yielded the smallest deviation from observed $FSCO_2$. While all three models have biases, the Taylor diagram for the monthly model is closer to the observed data points (Figure 8D). The quantiles of both the monthly and daily models have lower errors (Figure 8A–C), which indicates that they have strong predictive performance. Overall, the results suggest that the Monthly random effect model is the best model and can explain the most variation in the dependent variable of $FSCO_2$. It also adheres to the assumption that the variance of the errors is constant across all levels of the independent variable in a linear regression model.

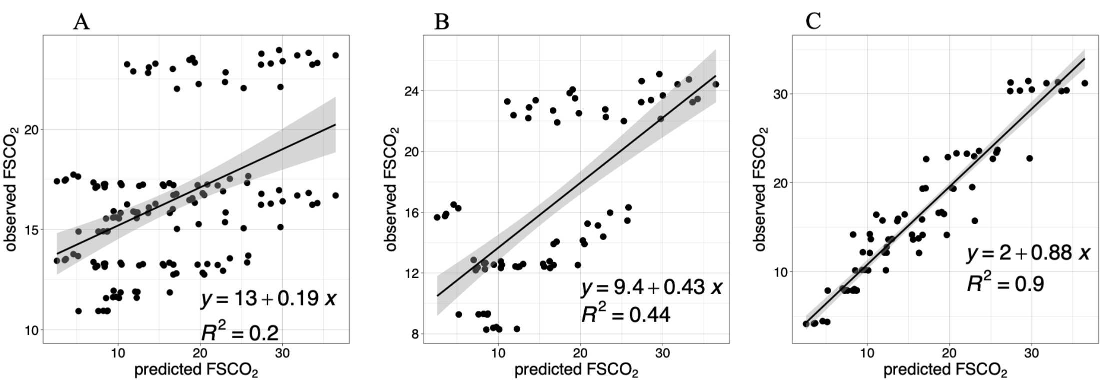

Figure 7. Predicted and estimated values of linear mixed models grouped by Month (**A**), Season (**B**) and Day (**C**) in the subtropical forest region.

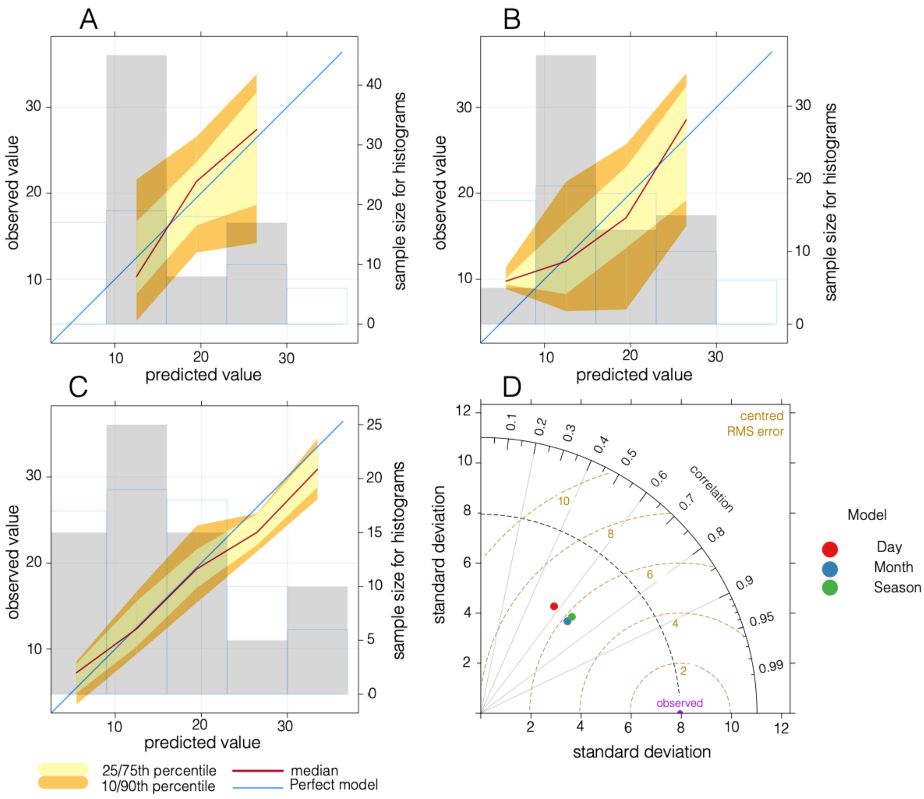

Figure 8. Conditional quantile plot to compare the three models (Season (**A**), Month (**B**) and Day (**C**)) and their post-processed combinations with respect to the observed data in terms of distribution and Taylor diagram to compare the three models (**D**).

4. Discussion

4.1. Spatial Heterogeneity of $FSCO_2$ Variations and Relationship between the Abiotic Factors

Based on the linear mixed effect models (e.g., Monthly random effect model), we mapped $FSCO_2$ spatial distribution during the study periods, and further calculated the pixel-based mean and slope values of $FSCO_2$ in the dry, autumn, and winter seasons to understand the spatiotemporal distribution characteristics of $FSCO_2$ in the subtropical region during the dry season (Figure 9). The mean $FSCO_2$ values in different seasons have small $FSCO_2$ in the north and center of the study areas compared with other areas. However, the mean $FSCO_2$ is variable in different periods. The highest $FSCO_2$ occurred in Autumn and Winter. The variation trends of $FSCO_2$ also have significant variation in different study periods, and the changing dynamics is the highest in autumn compared to other periods.

The predicted $FSCO_2$ and abiotic factors have significant relationships in dry seasons. Moreover, the degree of relevance is different in GY and CHD. Figure 10 shows that predicted $FSCO_2$ and topsoil temperature and near-surface air temperature have significant positive relationships; however, the relationship between the $FSCO_2$ and soil respiration is very weak in the GY site, while no significant relationship exists in the CHD site. Moreover, the correlation coefficients ($p < 0.001$) in the GY site were significantly higher than those in the CHD, illustrating that topography influences the relationship between the $FSCO_2$ and abiotic environmental factors.

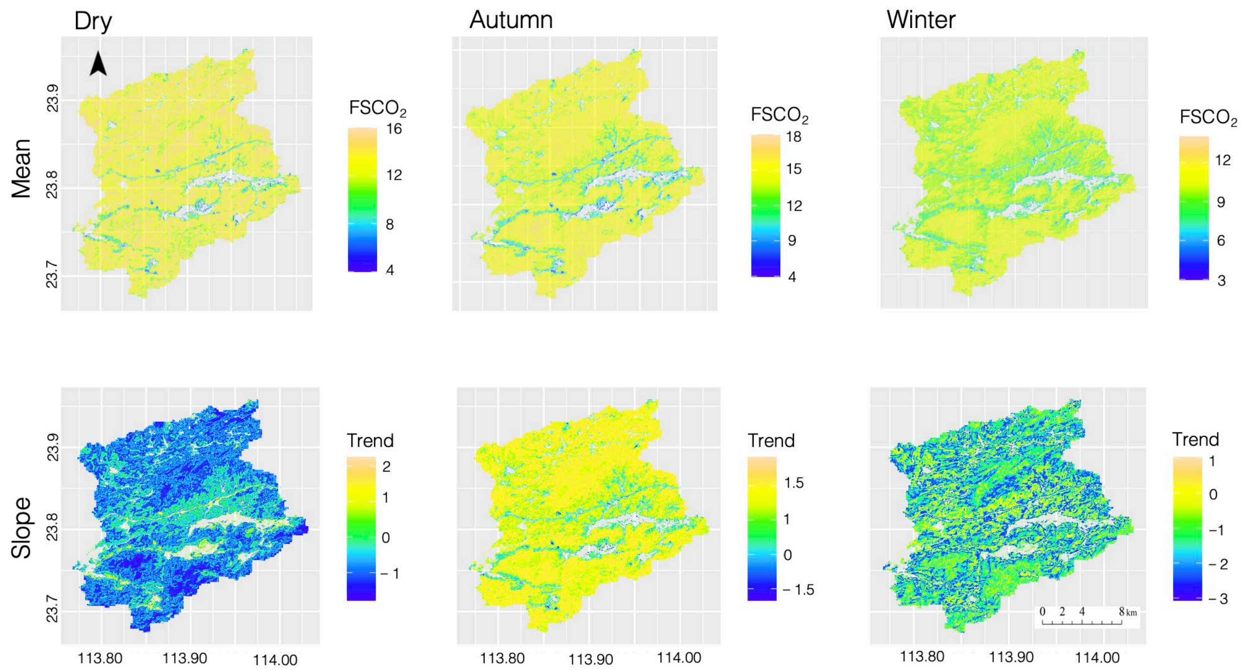

Figure 9. The spatiotemporal distribution patterns of the mean (Unit: g C m^{-2} day^{-1}) and trend values of $FSCO_2$ in the subtropical forest in dry seasons.

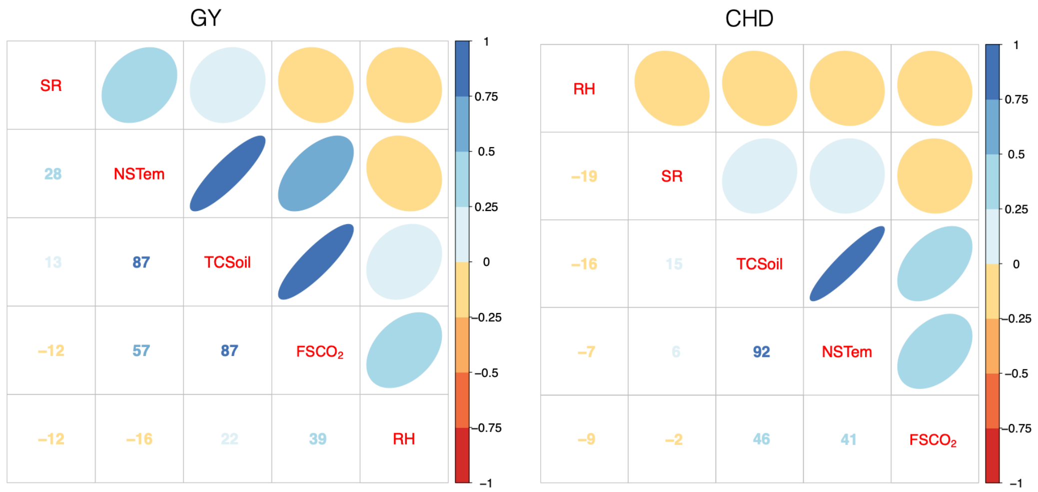

Figure 10. Relationship between the predicted $FSCO_2$ ($PFCO_2$) and environmental variables. GY refers to the GY site; CHD refers to the CHD site.

4.2. Spatiotemporal Dynamics of Soil CO_2 Efflux of Subtropical Forest in Dry Seasons

According to the results, the $FSCO_2$ during the dry season may offset a significant amount of CO_2 assimilated during the growing season, potentially accounting for 3–50% of annual carbon emissions. Therefore, $FSCO_2$ in the dry season is crucial to determine the annual carbon cycle [4,22,30,31]. In our study, the subtropical forest in dry seasons was targeted for using the remote sensing fusion method to acquire high-quality spatiotemporal products of *LST* and to estimate $FSCO_2$ in dry seasons. Our results indicated that $FSCO_2$ trended downward from 28 September to 4 January of the following year, which is consistent with the results of Chen et al. [22], who concluded that $FSCO_2$ has distinct variation during the dry season. Our results further revealed the spatiotemporal variability of $FSCO_2$ in dry seasons at high spatiotemporal resolutions, and significantly improved the distribution accuracy of $FSCO_2$ estimation. For example, at the temporal scale, we estimated daily $FSCO_2$ in the LXH reservoir basin. At spatial scales, we estimated 100 m spatial resolution of *$FSCO_2$* while significantly decreasing mixed-pixel uncertainty that would arise from coarse-spatial-resolution images. In addition, our estimated mean maximum and minimum values of *$FSCO_2$* in the autumn, winter, and dry seasons are lower than the estimated values by Chen et al. [22]. This discrepancy could be due to the following two reasons. First, there is a difference in the data sources for *$FSCO_2$* estimation. Chen et al. [22] used *MODIS* images at coarse 500 m spatial resolution that may have contained many mixed pixels that biased the true estimation of *$FSCO_2$*. Second, Chen et al. [22] assumed that the *$FSCO_2$* estimation values were affected by plant productivity and soil moisture but not land surface temperature. In our study, we aimed to mainly use the land surface temperature to improve the inversion accuracy of *$FSCO_2$* estimation at high temporal and spatial resolutions at regional scales. Nevertheless, our future study will add other biotic and abiotic factors, such as soil moisture and plant productivity, to further improve the model's accuracy. Moreover, our results revealed that the long spatiotemporal dynamics of *$FSCO_2$* experience daily, monthly and seasonal variability.

4.3. Remote Sensing Based Soil CO_2 Efflux Inversion

Remote sensing products are of great potential for the estimation of *$FSCO_2$* emission at long-time and large spatial scales [32]. Earth observation technology allows for the collection of data over large areas and over long time periods, making it well-suited for monitoring and estimating emissions at regional or global scales. Additionally, the use of remote sensing data can help to reduce the cost and logistic challenges associated with ground-based measurements. Freely accessible remote sensing images like Landsat, *MODIS*, and ASTER were commonly used in previous studies for estimating *$FSCO_2$* [10,32,33] and obtained a relatively optimistic accuracy in *LST* (Table 3). Wu et al. [3] reported long-time-series measurements of *$FSCO_2$* using the relationship between the *$FSCO_2$* and *MODIS LST*. Richard et al. [32] used nighttime and daytime *MODIS LST* data to monitor the *$FSCO_2$* for shorter time periods. Satellites equipped with thermal infrared detectors can be a valuable tool for measuring soil temperature at a large spatial scale, particularly in forested areas. This method can provide more accurate and extensive understanding of land surface temperature, and its potential impact on the environment, by circumventing the limitations of traditional in situ methods. It provides a more efficient and comprehensive approach to monitor soil temperature at landscape or ecosystem scales [3]. Richard et al. [32] assumed that satellite-remote-sensing-based *LST* values obtained from monitoring of the forest canopy can reflect forest canopy temperature. The forest canopy size plays a crucial role in determining the accuracy of *LST* estimation, as the heat retention capacity of the dense canopy during peak growth seasons is contingent on the air conditions in its immediate vicinity. Therefore, with an increase in forest canopy area, *LST* is close to the air temperature [32]. In our study, the forest canopy of the entire study area was greater than 98%. The Landsat-*MODIS LST* inversion therefore has a relatively positive relationship with air temperature, as shown in Figure 10.

Multisource remote sensing image fusion technology improves the quality of data by effectively fusing data from different sources and features, and by leveraging the unique advantages of various remote sensing data in terms of both spatial and temporal resolution. The calibration and verification of the fusion results can usually be achieved by using ground observation data. When it comes to using satellite technology to measure temperature on the earth's surface, we can obtain more accurate results by combining information from several different sources. We can achieve better precision by analyzing images that were acquired at different points in time, from varying perspectives, and at varying levels of radiation intensity [32]. In this study, that is why we used both Landsat and *MODIS LST* products to estimate high spatiotemporal *$FSCO_2$* at basin scales.

Table 3. Previous studies of remote-sensing-based soil CO_2 efflux monitoring during 2000–2022.

Authors	Sites	Method	Satellite Data and Resolutions	Inversion Spatial Scales	Highest Inversion Accuracy	Published Year
Kimball et al. [34]	Tundra forest	terrestrial carbon flux (TCF) model	*MODIS* and AMSR-E	Continent scale	0.89	2009
Huang et al. [35]	Broadleaf forest site (Midwest USA)	Statistical model	*MODIS LST*/500 m	Basin scale		2014
Wu et al. [3]	Canadian boreal black spruce stand	Linear regression model	*MODIS LST* & *NDVI*/500 m	Landscape scale	0.78	2014
Huang et al. [11]	FLUXNET forest	Remote-sensing-based model	*MODIS LST*/500 m	Site scale		2015
Huang et al. [36]	Croplands	support vector regression	Landsat 8 images	County level	0.73	2017
Ben Bond-Lamberty [37]		Artificial neural network model		Global scale		2018
Crabbe et al. [32]	Forest	Linear mixed model	Landsat 8 *LST*/30 m	Patch scale		2019
Warner et al. [38]	Bamboo forest	Quantile-based digital soil mapping	DEM/2 m	Basin scale	0.64	2019
Huang et al. [39]	Global	biome-specific statistical model	*MODIS*/1 km	Global scale		2020
Xu et al. [40]	Forest	Improved downscale model	*MODIS*, Landsat 8 OLI/TIRS	Regional scale	0.47	2020
Chen et al. [22]	Tropical forest	Random forest	*MODIS*/500 m	Basin scale	0.88	2021
Burdun et al. [33]	Peatlands	Model	Landsat/*MODIS LST*/1 km	Regional scale	0.67	2021

4.4. Accuracy Analysis of Remote Sensing Modeling for $FSCO_2$ Estimation

The high spatiotemporal simulation of the carbon flux between the surface and the atmosphere depends heavily on the field in situ observation of carbon flux. However, regional or general climate models ignore scale issues when monitoring carbon fluxes at a coarser scale. This limits our large-scale and high spatiotemporal retrieval of carbon flux at the soil-air interface. Our method provides an opportunity to estimate large-scale $FSCO_2$ from surface temperatures determined from the fusion of multisource satellite imagery.

The accuracy of $FSCO_2$ estimation based on satellite remote sensing images is subject to several factors, including satellite access time, specific distribution characteristics, regional topographic conditions, vegetation coverage, soil and air temperature, etc. [32]. The assessment of soil $FSCO_2$ in this study shows that soil moisture and temperature in the subtropical forests in the dry season are the main drivers of $FSCO_2$ change. It also indicated that the relationship between soil moisture and $FSCO_2$ is more complex than the relationship between soil temperature and $FSCO_2$. In other words, different degrees of soil wetness may apply different effects on the $FSCO_2$ efflux. The soil moisture (<50%) has a positive effect on $FSCO_2$ efflux for the subtropical forests in the dry season [22]. Another study found that the accuracy of estimating vegetation indices such as *NDVI*, LAI, and *LST* from satellite imagery is subject to soil moisture. The models developed in this study took this into account [3]. Previous studies have shown that oversaturated soil has a limiting effect on soil CO_2 release [3,32,33]. It is generally recognized that soil moisture in subtropical humid regions is relatively high and rainfall is sufficient. Therefore, for this reason, we have chosen the dry season (September to January of the following year) as the observation period. There was no rain in the study area during the study period, and the average soil moisture of the two sites was 18.10% and 20.99%, both less than 50%. Therefore, there was a positive correlation between $FSCO_2$ and soil moisture. Specifically incorporating soil moisture as a model parameter into a monthly model (Monthly random effect model) (at least when considering summer $FSCO_2$ variability) is necessary. However, the lack of high-quality soil moisture data with high spatial resolution limited this study. Therefore, improving the model using soil moisture from satellite remote sensing data is needed in future research.

4.5. Limitations and Future Works

This work attempts to deal with the accurate calculation of $FSCO_2$ at large spatial scales in a subtropical forest based on high spatiotemporal *LST* inversions. In other words, it provides an opportunity to estimate $FSCO_2$ at large spatial scales based on the surface temperature as determined by satellite remote sensing images. Although remote sensing fusion technology enables high temporal resolution for $FSCO_2$ estimation, there are still several limitations that need further addressing. Firstly, field measurement of $FSCO_2$ used chambers at five different times a day. *LST* is very sensitive to the air and soil temperature, and although we acquired quite satisfactory results from models, a better method should use the data with timing corresponding well with the satellite accessing time. Secondly, this paper collected observation data from two sites over a period of five months. The limited duration of the observations may have resulted in a relatively low accuracy of the model. Future research will attempt to improve the model by expanding the spatial and temporal scale of the observation data.

5. Conclusions

Utilizing satellite remote sensing images for $FSCO_2$ estimation has significance for accurate calculation of the carbon budget balance. Accurate spatiotemporal $FSCO_2$ estimation at regional scales is an urgent issue that needs immediate solutions for regional climate models. In this research, we estimated soil CO_2 efflux using a combination of Landsat and *MODIS* imagery and constructed linear mixed effect models that account for daily, monthly, and seasonal variability in Landsat-*MODIS* Fusion *LST* in the dry season. By using daily, monthly, and seasonal $FSCO_2$ measurements as separate random factors in the linear mixed effect model, three different $FSCO_2$ models were built. Our findings revealed that the monthly random effect model, which utilizes Landsat 8 *LST* and *MODIS LST* fusion images, can best explain the forest $FSCO_2$ dynamics at a regional scale. There is a strong positive correlation between the predicted $FSCO_2$ and abiotic environmental factors such as air and soil temperature. Future research can enhance these models by incorporating other biotic and abiotic factors such as plant productivity, soil moisture, etc. The estimation of soil CO_2 emissions from subtropical forests based on remote sensing is still in its infancy, and, to a large extent, this study deepened the knowledge of this field.

Supplementary Materials: The following supporting information can be downloaded at: https://www.mdpi.com/article/10.3390/rs15051415/s1, Figure S1: Spatial distribution of *LST* derived from multisource remote sensing images in different study periods of subtropical forests in dry seasons. First line is Landsat 8 *LST*, second line is *MODIS LST*, third line is Landsat-*MODIS* Fusion *LST*; Table S1: Linear mixed effect of which Fusion *LST* estimate grouped by month (random intercept effect) of observation was used to explain variability in soil $FSCO_2$ subtropical forests; Table S2: Linear mixed effect of which Fusion *LST* estimate grouped by season (random intercept effect) of observation was used to explain variability in soil $FSCO_2$ subtropical forests; Table S3: Linear mixed effect of which Fusion *LST* estimate grouped by day (random intercept effect) of observation was used to explain variability in soil $FSCO_2$ subtropical forests.

Author Contributions: Conceptualization, X.A. and G.T.; Data curation X.A., R.S. and N.E.; Methodology, X.A. and N.E.; Formal analysis, X.A.; Writing—original draft, X.A.; Writing—review & editing, X.A., G.T., C.H. and N.E.; Funding acquisition, X.A. and G.T.; Project administration, X.A., G.T. and C.H.; Software, X.A. and N.E.; Visualization, X.A., R.S. and N.E. All authors have read and agreed to the published version of the manuscript.

Funding: This work is supported by a grant from the National Natural Science Foundation of China (NO. 42171025), the State Key Laboratory of Resources and Environmental Information System and the Guangdong Natural Science Foundation Program (No. 2023A1515012069).

Data Availability Statement: All datasets used in the present study are available on request from the corresponding author.

Acknowledgments: The authors would like to thank the United States Geological Survey (USGS) and the Oak Ridge National Laboratory Distributed Active Archive Center (DAAC) for providing Landsat 8 and *MODIS* images respectively at no cost. We also express our gratitude to Zhenwu Xu and Tao Chen for their participation in collecting field data. Furthermore, we extend our special thanks to the editor and three anonymous reviewers for their valuable time and efforts in reviewing our work.

Conflicts of Interest: The authors declare no conflict of interest.

References

1. Crabbe, R.A.; Dash, J.; Rodriguez-Galiano, V.F.; Janous, D.; Pavelka, M.; Marek, M.V. Extreme warm temperatures alter forest phenology and productivity in Europe. *Sci. Total Environ.* **2016**, *563*, 486–495. [CrossRef] [PubMed]
2. Pumpanen, J.; Kolari, P.; Ilvesniemi, H.; Minkkinen, K.; Vesala, T.; Niinisto, S.; Lohila, A.; Larmola, T.; Morero, M.; Pihlatie, M.; et al. Comparison of different chamber techniques for measuring soil CO_2 efflux. *Agric. For. Meteorol.* **2004**, *123*, 159–176. [CrossRef]
3. Wu, C.Y.; Gaumont-Guay, D.; Black, T.A.; Jassal, R.S.; Xu, S.G.; Chen, J.M.; Gonsamo, A. Soil respiration mapped by exclusively use of *MODIS* data for forest landscapes of Saskatchewan, Canada. *ISPRS J. Photogramm.* **2014**, *94*, 80–90. [CrossRef]
4. Monson, R.K.; Lipson, D.L.; Burns, S.P.; Turnipseed, A.A.; Delany, A.C.; Williams, M.W.; Schmidt, S.K. Winter forest soil respiration controlled by climate and microbial community composition. *Nature* **2006**, *439*, 711–714. [CrossRef]
5. Borken, W.; Xu, Y.J.; Davidson, E.A.; Beese, A. Site and temporal variation of soil respiration in European beech, Norway spruce, and Scots pine forests. *Glob. Chang. Biol.* **2002**, *8*, 1205–1216. [CrossRef]
6. Katayama, A.; Endo, I.; Makita, N.; Matsumoto, K.; Kume, T.; Ohashi, M. Vertical variation in mass and CO_2 efflux of litter from the ground to the 40m high canopy in a Bornean tropical rainforest. *Agric. For. Meteorol.* **2021**, *311*, 108659. [CrossRef]
7. Makita, N.; Kosugi, Y.; Sakabe, A.; Kanazawa, A.; Ohkubo, S.; Tani, M. Seasonal and diurnal patterns of soil respiration in an evergreen coniferous forest: Evidence from six years of observation with automatic chambers. *PLoS ONE* **2018**, *13*, e0192622. [CrossRef]
8. Fu, G.; Shen, Z.; Zhang, X.; Shi, P.; Zhang, Y.; Wu, J. Estimating air temperature of an alpine meadow on the Northern Tibetan Plateau using *MODIS* land surface temperature. *Acta Ecol. Sin.* **2011**, *31*, 5. [CrossRef]
9. Yan, J.X.; Zhang, X.; Liu, J.; Li, H.J.; Ding, G.W. *MODIS*-Derived Estimation of Soil Respiration within Five Cold Temperate Coniferous Forest Sites in the Eastern Loess Plateau, China. *Forests* **2020**, *11*, 131. [CrossRef]
10. Ai, J.L.; Jia, G.S.; Epstein, H.E.; Wang, H.S.; Zhang, A.Z.; Hu, Y.H. *MODIS*-Based Estimates of Global Terrestrial Ecosystem Respiration. *J. Geophys. Res. Biogeo.* **2018**, *123*, 326–352. [CrossRef]
11. Huang, N.; Gu, L.H.; Black, T.A.; Wang, L.; Niu, Z. Remote sensing-based estimation of annual soil respiration at two contrasting forest sites. *J. Geophys. Res. Biogeosci.* **2015**, *120*, 2306–2325. [CrossRef]
12. Rozenstein, O.; Qin, Z.H.; Derimian, Y.; Karnieli, A. Derivation of land surface temperature for Landsat-8 TIRS using a split window algorithm. *Sensor* **2014**, *14*, 11277. [CrossRef]
13. Aliabad, F.A.; Zare, M.; Malamiri, H.G. A comparative assessment of the accuracies of split-window algorithms for retrieving of land surface temperature using Landsat 8 data. *Model. Earth Syst. Environ.* **2021**, *7*, 2267–2281. [CrossRef]
14. Du, C.; Ren, H.Z.; Qin, Q.M.; Meng, J.J.; Zhao, S.H. A practical split-window algorithm for estimating land surface temperature from Landsat 8 data. *Remote Sens.* **2015**, *7*, 647–665. [CrossRef]
15. Yu, X.L.; Guo, X.L.; Wu, Z.C. Land Surface temperature retrieval from Landsat 8 TIRS-Comparison between radiative transfer equation-based method, split window algorithm and single channel method. *Remote Sens.* **2014**, *6*, 9829–9852. [CrossRef]
16. Yan, L.; Li, H.; Han, Y.; Chen, J. Surface temperature splicing study fusing *MODIS* and Landsat 8: A case study in the Guangdong-Hong Kong-Macao Greater Bay. *Trop. Geogr.* **2015**, *39*, 689–700.
17. Hazaymeh, K.; Hassan, Q.K. Fusion of *MODIS* and Landsat-8 surface temperature images: A new approach. *PLoS ONE* **2015**, *10*, e0117755. [CrossRef]
18. Inamdar, A.K.; French, A.; Hook, S.; Vaughan, G.; Luckett, W. Land surface temperature retrieval at high spatial and temporal resolutions over the southwestern United States. *J. Geophys. Res. Atmos.* **2008**, *113*, D07107. [CrossRef]
19. Wu, M.Q.; Wu, C.Y.; Huang, W.J.; Niu, Z.; Wang, C.Y.; Li, W.; Hao, P.Y. An improved high spatial and temporal data fusion approach for combining Landsat and *MODIS* data to generate daily synthetic Landsat imagery. *Inf. Fusion* **2016**, *31*, 14–25. [CrossRef]
20. Yin, Z.X.; Wu, P.H.; Foody, G.M.; Wu, Y.L.; Liu, Z.H.; Du, Y.; Ling, F. Spatiotemporal fusion of land surface temperature based on a convolutional neural network. *IEEE Trans. Geosci. Remote Sens.* **2021**, *59*, 1808–1822. [CrossRef]
21. Zhu, Z.; Liu, B.J.; Wang, H.L.; Hu, M.C.A. Analysis of the spatiotemporal changes in watershed landscape pattern and its influencing factors in rapidly urbanizing areas using satellite data. *Remote Sens.* **2021**, *13*, 1168. [CrossRef]

22. Chen, T.; Xu, Z.W.; Tang, G.P.; Chen, X.H.; Fang, H.; Guo, H.; Yuan, Y.; Zheng, G.X.; Jiang, L.L.; Niu, X.Y. Spatiotemporal monitoring of soil CO_2 efflux in a subtropical forest during the dry season based on field observations and remote sensing imagery. *Remote Sens.* **2021**, *13*, 3481. [CrossRef]
23. Wang, S.; Qian, X.; Han, B.P.; Luo, L.C.; Ye, R.; Xiong, W. Effects of different operational modes on the flood-induced turbidity current of a canyon-shaped reservoir: Case study on Liuxihe Reservoir, South China. *Hydrol. Process.* **2013**, *27*, 4004–4016. [CrossRef]
24. Fleck, D.; He, Y.; Alexander, C.; Jacobson, G.; Cunningham, K.L. *Simultaneous Soil Flux Measurements of Five Gases—N_2O, CH_4, CO_2, NH_3, and H_2O—With the Picarro G2508*; Picarro Inc.: Santa Clara, CA, USA, 2013; pp. 1–11. Available online: https://www.picarro.com/support/library/documents/an034_simultaneous_soil_flux_measurements_of_five_gases_n2o_ch4_co2_nh3 (accessed on 1 September 2018).
25. Montanaro, M.; Gerace, A.; Lunsford, A.; Reuter, D. Stray light artifacts in imagery from the Landsat 8 thermal infrared sensor. *Remote Sens.* **2014**, *6*, 10435–10456. [CrossRef]
26. Barsi, J.A.; Schott, J.R.; Hook, S.J.; Raqueno, N.G.; Markham, B.L.; Radocinski, R.G. Landsat-8 thermal infrared sensor (TIRS) vicarious radiometric calibration. *Remote Sens.* **2014**, *6*, 11607–11626. [CrossRef]
27. Jimenez-Munoz, J.C.; Sobrino, J.A.; Skokovic, D.; Mattar, C.; Cristobal, J. Land surface temperature retrieval methods from Landsat-8 thermal infrared sensor data. *IEEE Geosci. Remote Sens. Lett.* **2014**, *11*, 1840–1843. [CrossRef]
28. Tang, S.M.; Wang, C.J.; Wilkes, A.; Zhou, P.; Jiang, Y.Y.; Han, G.D.; Zhao, M.L.; Huang, D.; Schonbach, P. Contribution of grazing to soil atmosphere CH_4 exchange during the growing season in a continental steppe. *Atmos. Environ.* **2013**, *67*, 170–176. [CrossRef]
29. Nakagawa, S.; Schielzeth, H. A general and simple method for obtaining R^2 from generalized linear mixed-effects models. *Methods Ecol. Evol.* **2013**, *4*, 133–142. [CrossRef]
30. Monson, R.K.; Sparks, J.P.; Rosenstiel, T.N.; Scott-Denton, L.E.; Huxman, T.E.; Harley, P.C.; Turnipseed, A.A.; Burns, S.P.; Backlund, B.; Hu, J. Climatic influences on net ecosystem CO_2 exchange during the transition from wintertime carbon source to springtime carbon sink in a high-elevation, subalpine forest. *Oecologia* **2005**, *146*, 130–147. [CrossRef]
31. Wang, W.; Peng, S.S.; Wang, T.; Fang, J.Y. Winter soil CO_2 efflux and its contribution to annual soil respiration in different ecosystems of a forest-steppe ecotone, north China. *Soil Biol. Biochem.* **2010**, *42*, 451–458. [CrossRef]
32. Crabbe, R.A.; Janous, D.; Darenova, E.; Pavelka, M. Exploring the potential of LANDSAT-8 for estimation of forest soil CO_2 efflux. *Int. J. Appl. Earth Obs.* **2019**, *77*, 42–52. [CrossRef]
33. Burdun, I.; Sagris, V.; Mander, U. Relationships between field-measured hydrometeorological variables and satellite-based land surface temperature in a hemiboreal raised bog. *Int. J. Appl. Earth Obs.* **2019**, *74*, 295–301. [CrossRef]
34. Kimball, J.S.; Jones, L.A.; Zhang, K.; Heinsch, F.A.; McDonald, K.C.; Oechel, W.C. A Satellite Approach to Estimate Land-Atmosphere CO_2 Exchange for Boreal and Arctic Biomes Using *MODIS* and AMSR-E. *IEEE Trans. Geosci. Remote Sens.* **2009**, *47*, 569–587. [CrossRef]
35. Huang, C.; Chen, Y.; Wu, J.P. Mapping spatio-temporal flood inundation dynamics at large river basin scale using time-series flow data and *MODIS* imagery. *Int. J. Appl. Earth Obs.* **2014**, *26*, 350–362. [CrossRef]
36. Peng, Y.D.; Li, W.S.; Luo, X.B.; Du, J.; Zhang, X.Y.; Gan, Y.; Gao, X.B. Spatiotemporal reflectance fusion via tensor sparse representation. *IEEE Trans. Geosci. Remote Sens.* **2022**, *60*, 1–18. [CrossRef]
37. Bond-Lamberty, B. New techniques and data for understanding the global soil respiration flux. *Earths Future* **2018**, *6*, 1176–1180. [CrossRef]
38. Warner, D.L.; Guevara, M.; Inamdar, S.; Vargas, R. Upscaling soil-atmosphere CO_2 and CH_4 fluxes across a topographically complex forested landscape. *Agric. For. Meteorol.* **2019**, *264*, 80–91. [CrossRef]
39. Huang, N.; Wang, L.; Song, X.P.; Black, T.A.; Jassal, R.S.; Myneni, R.B.; Wu, C.Y.; Wang, L.; Song, W.J.; Ji, D.B.; et al. Spatial and temporal variations in global soil respiration and their relationships with climate and land cover. *Sci. Adv.* **2020**, *6*, eabb8508. [CrossRef]
40. Xu, C.Y.; Qu, J.J.; Hao, X.J.; Zhu, Z.L.; Gutenberg, L. Monitoring soil carbon flux with in-situ measurements and satellite observations in a forested region. *Geoderma* **2020**, *378*, 114617. [CrossRef]